

# How wide spread deflections bias brain-wide models of resting state fMRI.

Kevin M. Aquino<sup>1,\*</sup>, Gustavo Deco<sup>1,2</sup>, Leonardo Gollo<sup>1</sup>, Stuart Oldham<sup>1</sup>, Ben Fulcher<sup>3</sup>, and Alex Fornito<sup>1</sup>

<sup>1</sup>The Turner Institute for Brain and Mental Health, School of Psychological Sciences, and Monash Biomedical Imaging, Monash University, Victoria, Australia.

<sup>2</sup>Universitat Pompeu Fabra, Barcelona, Spain.

<sup>3</sup>USYD, Sydney, Australia.

**Large-scale dynamics of the brain are routinely modelled using systems of dynamical equations that describe the evolution of population-level activity under certain biophysical constraints, and are coupled according to an empirically measured structural connection matrix. This modelling approach has been used to generate insights into the neural underpinnings of spontaneous brain dynamics, as recorded with techniques such as resting state functional MRI (fMRI). However, parallel studies into the fMRI have revealed a wealth of structured noise – from small to large scale – and has revealed a lack of a consensus of which pre-processing and de-noising steps should be used. The specific choice of pre-processing models has a major impact on the final measures that compare population groups and understand underlying biology of human cortex, but these impacts are rarely considered in the modelling sphere. We show, using popular neural mass models, that key de-noising step leads to very different degrees of model fit and interpretations of findings. These results question estimates of reported model parameters, model interpretation, and, in the worst case, model validity. We try to bridge the gap between theory and experiment by presenting recent quality control measures on the acquired data and the different types of structured noise. We hope to open the dialog between the modelling and experimental rsfMRI communities, which is necessary to advance our understanding of the resting brain.**

resting-state | fMRI | denoising | modelling | network | DiCER | GSR | rsfMRI

Correspondence: kevin.aquino@monash.edu

## Introduction

Over the last three decades, functional magnetic resonance imaging (fMRI) has focused on understanding the brain at “rest” or more specifically task-free. Imaging the brain in this state is sought to provide researchers an insight into the brain’s idling dynamics - the default mode of the brain. Imaging the brain “at rest” is attractive paradigm as it can be easily acquired in the healthy population and has replaced many task-based analyses between groups where a balanced task response between patient groups and controls is difficult or in some cases impossible to develop (REFs).

Resting state fMRI has led to the discovery that the brain at rest exhibits synchronized fluctuations, revealing resting state networks (1) that are robustly detected across individuals and species (2, 3) (+Monkey and mice papers). These resting state networks are unique enough between individuals to allow subject identification (4, 5), are related to independent behavioural measures (6) and the associated correlation structure is related to the underlying neural connec-

tivity (Messe+Hagmann et al.). For these reasons resting state fMRI (rsfMRI) has potential promise in the clinical domain, as resting-state connectivity patterns are different between patient groups (REFs), change in response to treatment (REFs), and thus serve as potential biomarkers.

There are many open questions as to the meaning of these networks, such as: what is driving these resting state fluctuations? (REFs) Does anatomical structure drive these co-ordinated flucations? (REFs) What drives differences between patient groups (Need refs for all of these). Large-scale biophysical models of cortical activity have sought to bridge the gaps in our understanding and have attempted to answer these questions. The majority of these models are at the mesoscopic population level, where the populations are on the scale of units derived from parcellations of cortex (REFs) and subcortex. The aim of these models is to simulate the resting brain and reproduce the functional connectivity network, where the nodes are the population units and the edges detail the empirical connectivity typically from correlations between nodes. Specifically, these are embodied in a functional connectivity (FC) matrix. These models have three critical ingredients - a biophysically realistic model of population dynamics, an anatomically defined connectivity structure, and a set of meaningful parameters.

Firstly, at each node is a model that describes the net neural activity from a small patch of cortex. The translation from single neurons to a population are typically derived via neural mass (REFs) or neural field theory (REFs). Recent models have also been derived that capture the canonical dynamics that come both these theories - i.e. noisy oscillations described by a Hopf bifurcation (REFs Freyer, Robers, Gustavo). Although the form of all of these models can be quite complex, resting state can be viewed as a perturbation from a steady state and thus allow many models to be linearized (to some extent), reducing the complexity allowing efficient computation. In addition, at each node many populations can be ascribed within a single unit e.g. excitatory, inhibitory, and associated populations through the lamination of cortex. The coupling to all other nodes are mediated through excitatory to excitatory connections. The resultant excitatory neural dynamics are then translated to a BOLD forward model that allows a direct simulation of resting state fMRI.

Secondly, coupling between nodes is imposed by anatomical connections that emulates how neurons are wired and exert influence to one another. This anatomical connectiv-

ity is usually defined from measurements that use diffusion weighted MRI and automated fibre tracking to and from each node (REF). These fibre tracks are undirected and summarized in a symmetric structural connectivity matrix that can detail the existence of connection between two nodes and/or the strength of this connection (REFs.). In some non-human modelling, asymmetric matrices can be utilized via experiments that use invasive recordings that can track directionality of fibre tracks. Importantly, it is worth noting that these matrices are limited in their resolution and accuracy specifically that inter-hemispheric connections are generally underestimated (REFs), have strong spatial dependence that roughly follows an exponential decay (REFs), and many modelling studies use an average structural connectivity matrix aggregated from many subjects.

Lastly, each biophysical model requires two types of parameters - at the global and at the individual node level. The global parameter/s are used to scale the anatomical connections uniformly as the structural connectivity matrix is calculated without units compatible with the models. In almost all models, this global parameter is a hyper parameter that has a large influence on the dynamics - scaling all connections too high can result in largely synchronized activity and too low causes asynchronous fluctuations. This is typically tuned to maximise model fits while being in a biologically relevant dynamic range. At the node level, the neural mass or neural field models use techniques that translate measured parameters from the neuronal scale to the mesoscopic scale. The first generation of these large-scale models use the same local parameters for each node (REFs), however with the advent of additional measurements - such as intracortical myelin markers (REFs) - recent models employ heterogenous population parameters that have improved model fitting. (see below).

Through the application to rsfMRI, large-scale biophysical modelling has found that structure largely guides functional connectivity in both humans (REF) and primates (REF). The accuracy of such modelling is usually determined by how well it can reproduce the functional connectivity matrix, and models have increased their accuracy as models have become more sophisticated and imaging has improved. Recently, there has been a shift to use additional metrics on simulated and empirical data to further investigate model accuracy and validity by using dynamic measures such as using time varying functional connectivity, metastability, and phase coherence (REFs add more?). In concert, additional parameters are being allowed to vary to fit to these dynamic measures which has provided estimates of directed structural connectivity by allowing the structural connectivity to vary (DCM REFs, Gilson Refs) and estimates of brain wide variation of neural populations by allowing local node parameters to vary (REFs). These recent developments allow estimates of parameters that indirectly measure neuromodulatory process, which provide further generative insights, understand the implications of neural deficits, and these parameters have potential to be biomarkers that are directly related to neural processes.

The ease of recording rsfMRI, and the suitability to many

biophysical models has seen the acceleration of studies acquiring and investigating the brain at rest. However, with this advance, recent studies have revealed a wealth of confounding artefacts within rsfMRI such as the presence of widespread deflections (WSDs) correlated to head motion (REF), heart rate variability (REF), respiration (REF), time of acquisition (REF). Although there have been efforts over the last 30 years to remove these effects through physiological modelling (RETROICOR REF), improved motion correction algorithms (REF), fMRI acquisition advancements (ME ref), and advancements in de-noising (MANY REFs) there is a large influence of motion and physiological confounds on rsfMRI. This is most clearly manifested in popularized “carpet (or gray) plots” which show temporal relationships of these confounds with rsfMRI (Power, Glasser, Aquino). In practice, this results in high global correlations functional correlations where the strength of these correlations have been shown to relate to motion (REF) or physiology (REF) making neural inferences from rsfMRI difficult to separate from these processes. This issue is important in groups that naturally have differences in head motion (REFS) or physiology (REFS) which make neuronal differences harder to determine. Through these confounds, there does not appear to be a clear consensus on the appropriate steps for not just de-noising but the order and type of steps with pre-processing pipelines - however there is a growing movement to standardize many of these steps (fMRIprep reference) and to utilize large unified sources of data.

Ongoing efforts within the rsfMRI community have placed greater standards that analyze not just group-level metrics but capture artefacts at the individual level by analyzing spatiotemporal time series via carpet plots (REFS) and quality control (QC) metrics that measure the influence of motion or respiration on FC edges. These tools are being employed to critically evaluate existing and new tools that denoise fMRI data and are often used to question any denoising method (7, 8)

However, the modelling community has largely ignored these significant challenges within experimental rsfMRI. Equivalent comprehensive investigations on the effects of pre-processing, de-noising techniques, the visualisation of carpet plots or QC metrics have not penetrated the investigation of model outputs or inferences. Although the use of one particular de-noising strategy - global signal regression (GSR) - has been discussed (Messe and others papers), its use or non-use is not standard and largely model dependent. Therefore, there is a gap in the field to determine whether WSDs influence model prediction, whether motion or respiration influences model estimates, and if WSDs influence model validity.

++ Working on a table of other papers and summarizing: the model, the study, MPP used, De-noising strategies, and QC for each model. Basically want to emphasize that nothing comprehensive has been done for any of these studies. ++

Here, we investigate the effects of WSDs on modelling by employing recent techniques in the rsfMRI literature to a set of XX existing large-scale biophysical models. We find that the existence of WSDs influence model fits to a sig-

nificant degree, and find that in some models increasing the accuracy/level of de-noising methods reduces model fits across many models. We find that many models are biased to modelling large scale coherent activity that is impossible (with many current methods) to disambiguate from potential sources of physiological or motion-driven noise. Second order neuronal fluctuations i.e. those that are not global do not fit very well on most models thus, we find that models need to be improved on the whole. We demonstrate this issue of bias to WSDs by showing that we can reduce down a recent model to a linear operation of degree and noise that outperforms models in terms of static FC and dynamic FC. We do find however, that heterogeneity can improve model accuracy and model second order effects that are less prone to WSDs driven by motion or physiology at the cost of model complexity. All analysis here is provided in open source toolboxes at XXX.

## Imaging Methods

### Resting state fMRI.

Here, we used transparent, open rsfMRI datasets processed using open-source pipelines from `fmriprep` (9) and the Human Connectome Project (HCP) (10).

**Imaging data & preprocessing.** We utilized three open source data sets from the healthy controls of the UCLA Consortium for Neuropsychiatric Phenomics LA5c Study (11) ([v00016 openneuro.org/datasets/ds000030/](https://openneuro.org/datasets/ds000030/)), the Beijing-Zang dataset (`fcon_1000.projects.nitrc.org/fcpClassic/FcpTable.html`) and resting state fMRI from the HCP. The scanning parameters for these three datasets are described in (9), [http://fcon\\_1000.projects.nitrc.org/fcpClassic/FcpTable.html](http://fcon_1000.projects.nitrc.org/fcpClassic/FcpTable.html) and (10), respectively; a brief summary is presented in Table 1.

“Minimal” preprocessing pipelines were used on the three datasets, where the UCLA and BZ datasets were processed using `fmriprep` v1.1.1 as described in (12). Briefly, this involves processing the T1-weighted anatomical images that involve: bias field correction, brain extraction, freesurfer segmentation, and volume normalization to the MNI 152 Nonlinear Asymmetric template version 2009c (13). On the functional MRI, the minimal preprocessing steps involve: slice time correction, motion correction, distortion correction using a template based  $B_0$  image, and co-registration to the T1 anatomical image. The versions of code, and specific details of the algorithms are detailed in the code described above and in (12). Functional imaging data from the HCP data were minimally preprocessed in a similar fashion, using the minimal HCP pipelines described in Glasser et al. (14) which additionally describes how the data were projected data into “grayordinates” which compactly represent data from grey matter cortex and subcortex in a dedicated structure. These grayordinates are described on a normalized template that has been surface registered for cortex data using the Multimodal Sulcal Matching (MSM) algorithm, and volume-registered using `fnIRT` (15) (check ref) to MNI 152

space for subcortex data. The purpose of having two different pipelines was to use established data that have already undergone quality control so that these QC measures can be analyzed in the context of modelling, and represents typical data in clinical studies (UCLA and BZ) and data in the general population (HCP). In addition, the comparisons owing to de-noising levels are only to be interpreted within each dataset as site effects between scanning is a major confound to functional connectivity measures.

For transparency, the code to re-run all of these analyses are located at <https://github.com/BMHLab/DiCER.git>, and in the following sections we describe de-noising strategies that follow minimal preprocessing. In our de-noising strategies we utilize two streams employed to the two sets of data.

**De-noising strategies for UCLA and BZ.** Firstly, for UCLA and BZ, Functional MRI data were analyzed within the MNI 152 Asymmetric 2009c space, which has been resampled to the native BOLD imaging dimensions, and we resampled any remaining anatomical masks/images to this space (including those that were not automatically resampled in the `fmriprep` workflow).

We restrict our analysis to gray-matter voxels (GM), in UCLA and BZ, to minimize partial-volume effects, and we additionally restricted voxels contained within the GM probability masks (calculated in `fmriprep`) thresholded at > 50% probability. We also excluded voxels with signal intensities that were below 70% of the mean fMRI signal intensity to avoid contamination by voxels with low signal plagued by susceptibility and partial-volume effects.

ICA-based Automatic Removal Of Motion Artifacts (AROMA) was used to generate noise regressors for use in the non-aggressive variant of the method (16). Regressors were calculated on the spatially smoothed variant of the minimally preprocessed images (as described within `fmriprep` as a 6 mm FWHM kernel) and then applied to the unsmoothed preprocessed images,

Following ICA-AROMA, we extracted mean time courses from eroded masks (using a 3x3x3 erosion kernel) of the WM and CSF. The masks were generated by following Parkes et al. (8) and Power et al. (17), where CSF and WM ROIs were created from tissue probability maps in `fmriprep`. We eroded the WM mask five times and the CSF mask once. Erosion is crucial to avoid partial-volume effects from gray matter, which inflates the correlation between WM/CSF estimates and the global-mean signal (8, 18). We extracted these signals from the AROMA-denoised data, as performed in Pruij et al. (16).

The above steps are fairly standard and accepted de-noising techniques, however wide spread deflections (WSDs) are present following these pipelines which correlation structure is related to motion, corrupting neuronal inferences. Thus, further de-noising methods are implemented: Global signal regression (GSR), and Diffuse Cluster Estimation and Regression (DiCER) both of which has been shown to mitigate the influences of WSDs in different ways.

<b>Dataset</b>	<b>BOLD parameters</b>	<b>Volumes</b>	<b>Subjects</b>	<b>Notes</b>
UCLA LA5c Study (11)	TE = 30 ms, 3 mm Inplane resolution, 34 slices with 4 mm slice thickness, FA= 90, FOV= 192 mm, matrix = $64 \times 64$ , Oblique and interleaved Gradient echo EPI sequences, TR = 2 s	152	121	We focused on the healthy controls (from the original sample of 270 people), that included subjects aged 21–50.
Beijing-Zang <a href="http://fcon_1000.projects.nitrc.org/">http://fcon_1000.projects.nitrc.org/</a>	TE= 30 ms, 3.125 mm, Inplane resolution, 33 slices with 3.6 mm, slice thickness, FA= 90, FOV= 200 mm, matrix = $64 \times 64$	225	192	Subjects were healthy controls.
HCP	TE= 30 ms, 3.125 mm, Inplane resolution, 33 slices with 3.6 mm, slice thickness, FA= 90, FOV= 200 mm, matrix = $64 \times 64$	225	100	Subjects were unrelated healthy controls, with the same fMRI reconstruction.

**Table 1.** Summary of acquisition parameters for the functional MRI and structural MRI used in this study. Note: not all essential parameters were reported in the open repositories, we list those that were reported.

For GSR, we use the mean gray-matter signal as for the global signal since it is highly correlated to the mean signal from the entire brain and contributes the most to the signal (17, 19). We thus refer to regression of this signal from fMRI gray-matter regression (GMR) for clarity. The concept of GMR is that since this represents the mean wide-spread signal its removal will reduce WSDs.

As shown in (12), rsfMRI data following GMR are left with a wide variety of WSDs that are correlated to motion or physiology, which are revealed under a re-ordering of the conventional carpet plots. DiCER is a method that targets these WSDs by focusing on diffuse, weakly correlated clusters, and has revealed to improve statistical sensitivity within datasets. We utilize DiCER as described within Aquino et al. (12) to retrieve noise regressors.

Using the noise-signal estimates, we perform three noise corrections, with (i) regression with the WM and CSF physiological signals, denoted as ‘+2P’; and (ii) regression with WM, CSF and GM signals, denoted as ‘+2P+GMR’. (iii) regression with WM, CSF and DiCER regressors, denoted as ‘+2P+DiCER’. The first two models were applied after ICA-AROMA denoising in a single step using ordinary least squares regression implemented in `fsl_regress`, and the last model was applied post (i) as DiCER is targeting residual noise.

The data, including the minimally preprocessed data, were then detrended with a 2nd order polynomial and high-pass filtered at 0.005 Hz using AFNI’s 3dTproject. This procedure resulted in four datasets for each subject, labeled ‘MPP’, ‘ICA-AROMA+2P’, ‘ICA-AROMA+2P+GMR’, ‘ICA-AROMA+2P+DiCER’.

**De-noising strategies for HCP.** Post minimal preprocessing (MPP), rsfMRI from the HCP were de-noised with ICA-FIX (20, 21) which is an algorithm that uses spatial ICA to uncover a host of spatially independent components that are classified as noise or signal by a training algorithm. We use the de-noised data from the HCP (release xx?). As noted by

Power et al. (17), Glasser et al. (19) and Aquino et al. (12), this data still exhibits WSDs that are related to either motion, heart rate variability or respiration. GSR can mitigate some of these effects(22), but considerable artefacts can remain (12, 19). Here we additionally applied DiCER to the data from the HCP as way to additionally mitigate these effects as detailed in (12). However, in future a temporal ICA approach will be more suitable in future as detailed in (19). The data, including MPP, were then detrended with a 2nd order polynomial and high-pass filtered at 0.005 Hz using AFNI’s 3dTproject. This procedure resulted in four datasets for each subject, labeled ‘MPP’, ‘MPP+ICA+FIX’, ‘MPP+ICA-FIX+GMR’, ‘MPP+ICA-FIX+DiCER’.

Again, we stress that the results comparing differences in model fits can only be compared within each dataset as to remove well-known confounds of site, scanner quality and populations.

#### ***Node definition through Cortical and subcortical parcellation.***

***Structural connectivity matrix (SC).*** This was done by Stuart – have to fill in what has been done.

***Quality control methods and subject exclusion.*** In the reaction to the abundance of potential artefacts and number of rsfMRI scans, there has been a push to develop automatic quality control (QC) methods at the single-scan and group level.

At the single scan level, the spatiotemporal time series of fMRI is visualized with carpet plots (or “grayplots”) that involve a heat map that shows each voxel (or summary parcel) at each row, where the column entries are time points. On top of these measures are time series that are potential confounds - such as framewise displacement (FD), global signal, respiratory envelope, pulse pressure, or heart rate. WSDs appear as large bands within the gray plots and their identification as being influenced by physiology or due to motion by being occurring with the vicinity of spikes or changes within

the aforementioned traces. Besides changes in connectivity, de-noising techniques are often evaluated by their ability to remove WSDs in these carpetplots (17, 22, 23). Here, we utilize carpet plots under different orderings on the y-axis as random ordering (RO) of carpet plots under-emphasize the presence of WSDs and whether or not de-noising methods - such as GSR - has actually removed them (12). The additional orderings involve ordering the y-axis with respect to the correlation to the global signal (GSO), and orderings based on hierarchical clustering denoted as cluster ordering (CO) as implemented in (specific code?).

At the group level, we consider three analyses. Quality control-functional connectivity correlations (QC-FC), a commonly used benchmark (7, 8, 17), which is estimated as the cross-subject correlation between FC and mean FD at each edge in an FC network. The QC-FC quantifies the association between inter-individual variance in FC and gross head motion, indexed by mean FD (mFD). An efficient denoising method will be less corrupted by motion and hence score lower on this metric. The QC-FC is calculated throughout all edges, however the findings are summarized as counting the percentage of  $p < 0.05$  (uncorrected) edges in the QC-FC correlation matrix. Secondly, another signature of successful rsfMRI denoising is a reduced dependence of QC-FC on the separation distance between pairs of ROIs (8, 24). Thirdly, we note that we implicitly used the ‘flat’ appearance of carpet plots to demonstrate that an fMRI dataset does not contain large WSDs, and thus to estimate the success of a given denoising procedure. A quantification of this ‘flatness’ can be achieved by using the variance explained by the first principal component (PC) of the voxel  $\times$  time rsfMRI data matrix, denoted as ‘VE1’. High values of VE1 indicate that a large proportion of fMRI variance can be captured by a single component (PC1), consistent with the presence of dominant WSDs.

## Modelling Methods

Here, we use three established dynamical models that can reproduce rsfMRI connectivity patterns. These models are a subset of all available neural models but represent the most commonly used models in the literature. In general these models have a canonical form:

$$\frac{z_i}{dt} = f(\mathbf{z}, \theta_i, G, C), \quad (1)$$

where neural activity  $z_i(t)$  is described at node  $i$ , owing to a dynamical model  $f$  that depends on all other nodes (and populations)  $\mathbf{z}$ , with parameters  $\theta_i$ , structural connectivity matrix  $C$  scaled by global parameter  $G$ . Below we describe the details of each model as well as the parameters for each model.

**The balanced excitation-inhibition model.** The balanced excitation-inhibition model simulates the collective behavior of excitatory populations that are in balance with inhibitory populations using a mean field approach (DECO et al.). This model is an extension of the Wang et al model, that is guided by the experiments in primates that show that local neural

populations fire at a resting oscillation of 3Hz. This resting firing rate forms an additional constraint on the dynamics which is achieved by raising/lowering the excitatory-inhibitory ratio such that each node in the system has a mean firing rate of 3Hz. The model is set as a series of coupled stochastic differential equations evaluated at excitatory (E) and inhibitory populations (I):

$$I_i^E = W_E I_0 + w_+ J_N S_I^E \dots \\ \dots + G J_N \sum_j C_{ij} S_J^E \dots \\ \dots - J_i S_i^I + I_{external}, \quad (2)$$

$$I_i^I = W_I I_0 + J_N S_i^E - S_i^I, \quad (3)$$

$$\frac{dS_i^E(t)}{dt} = -\frac{S_i^E}{\tau_E} + (1 - S_i^E) \gamma r_i^E + \sigma \nu_i(t), \quad (4)$$

$$\frac{dS_i^I(t)}{dt} = -\frac{S_i^I}{\tau_I} + r_i^I + \sigma \nu_i(t), \quad (5)$$

$$r_i^E = H(E, I_i^E), \quad (6)$$

$$r_i^I = H(I, I_i^I), \quad (7)$$

$$H(x, y) = \frac{a_x y - b_x}{1 - \exp - d_x(a_x y - b_x)}, \quad (8)$$

where the variable  $I_i^{E,I}$  indicates ionic current,  $S_i^{E,I}$  denotes the average synaptic gating variable, and  $r_i^{E,I}$  denotes the population firing rate - where all these dynamic variables are described at excitatory and inhibitory populations ( $E, I$ ) at node  $i$ . The parameters  $W_E, W_I$  describe the overall scaling of the excitatory and inhibitory currents respectively,  $w_+$  describes the local excitatory recurrence,  $J_N$  is the excitatory synaptic coupling,  $\tau_{E,I}$  are time constants for excitatory and inhibitory populations,  $\gamma$  is a kinetic rate constant. The function  $H(x, y)$  is the neuronal input-output function for population  $x$  due to input current  $y$ , which is parameterized for population  $x$  with parameters  $a_x$ , and  $b_x$  and this function maps how the net current induces a population level firing rate. This model simulates resting state activity as the neural response to a noisy input  $\sigma \nu_i(t)$ , where  $\sigma$  scales the level of noise. The local dynamics are “balanced” by having the requirement that the local firing rate is 3Hz at each node - a requirement that is modelled by adjusting the ratio of the influence of the inhibitory populations parameterized by the parameter  $J_i$  and estimated numerically (see below). The parameters, and their nominal values are in table y.

The model is solved numerically with MATLAB, where the equations are solved using an Euler-Maryuami integration scheme. In addition the parameter  $J_i$  is estimated via a greedy search algorithm, where its value is raised or lowered so that each node meets the 3Hz firing rate conditions. See Deco et al. 2014 for more details, where the algorithmic implementation is placed in the code at XXXX. In addition, the output the synaptic gating  $S_E(t)$  is used as the input  $\rightarrow$  inputs to BOLD forward model

**Neural-mass model.** The neural-mass model simulates neuronal dynamics by a series of neuronal masses based off the

Hodgkin-Huxley model (REF). The main dynamical variables are the excitatory (V) and inhibitory (Z) membrane potentials as well as the fraction of open sodium channels (W). At the node  $i$  level, the dynamics are derived by using the equivalent electrical circuits of a neuron, averaged over a small patch of cortex, that describe the conductance of sodium (Na), potassium (K) and calcium ions (Ca). The dynamical equations are as follows:

$$\begin{aligned} \frac{dV^i}{dt} &= -[g_{\text{Ca}} + rQ_{\Sigma}^i] m_{\text{Ca}}^i (V^i - V_{\text{Ca}}) \dots \\ &\dots - (g_{\text{Na}} m_{\text{Na}}^i + Q_{\Sigma}^i) (V^i - V_{\text{Na}}) \dots \\ &\dots - g_{\text{K}} W^i (V^i - V_{\text{K}}) \dots \\ &\dots - g_L (V^i - V_L) \dots \\ &\dots - a_{ie} Z Q_Z^i + a_{ne} I, \end{aligned} \quad (9)$$

$$\frac{dW^i}{dt} = \frac{\phi}{\tau} (m_{\text{K}}^i - W^i), \quad (10)$$

$$\frac{dZ^i}{dt} = b (a_{ni} I + a_{ei} V^i Q_V^i), \quad (11)$$

$$Q_X^{(i)} = \frac{1}{2} \left\{ 1 + \tanh \left[ (X^{(i)} - X_T) / \delta_X^{(i)} \right] \right\}, \quad (12)$$

$$m_{\text{ion}}^i = \frac{1}{2} \left\{ 1 + \tanh \left[ (V^{(i)} - V_{\text{ion}}) / \delta_{\text{ion}} \right] \right\}, \quad (13)$$

where the firing rate  $Q_{V,Z}^i$  for excitatory and inhibitory populations are described via a sigmoid function that models the action potential at a population level which is parameterized by the mean population thresholds  $V_T, Z_T$ , and the variance of these thresholds  $\delta_{V,Z}$ . The parameter  $g_{\text{Na,Ca,K}}$  is the conductance of ion channels and  $r$  is the ratio of NMDA to AMPA receptors. The term  $m_{\text{ion}}^i$  is the ratio of the open to closed ion channels that is described according to a sigmoid, parameterized by the mean nerst potentials of the ion channels  $V_{\text{ion}}$  with the term  $\delta_{\text{ion}}$  capturing the variance of these potentials. The potassium channels is a special case that is dynamically modelled to relax to an additional state modelled as a exponential decay in Eq. 10 where the decay the parameter  $\tau$  is the relaxation rate and  $\phi$  is the temperature scaling factor. The parameters  $a_{ee}, a_{ei}, a_{ie}, a_{ne}, a_{ni}$  are the connection weights between inhibitory ( $i$ ), excitatory ( $e$ ), and external input ( $n$ ) populations. The external population is modelled simply as a population that has input ionic current  $I$ . In this model, leaky currents are included that dissipate the excitatory membrane potential with appropriate parameters (of conductance and nerst potential) with subscript  $L$ . At the node level (i.e. when there is no coupling -  $G = 0$ ), the solutions exhibit dynamics similar to a hindmarsh rose neural oscillator described by a xxx. The coupling between nodes ( $G > 0$ ) are mediated through excitatory projections where the net firing rate from the network onto a single node is given by

$$Q_{\Sigma}^i = (1-G) r a_{ee} Q_V^i + G r a_{ee} \sum_{j,j \neq i} Q_V^j \frac{C_{ij}}{D_i}, \quad (14)$$

where  $D_i$  is the degree of the node ( $D^i = \sum_j C_{ij}$ ), and  $Q_{\Sigma}$  modulates the contributions of Sodium and Calcium excitatory membrane potentials. These equations are a nonlinear

dynamical system that for realistic biophysical parameters and realitvely weak coupling, exhibits chaotic dynamics with weakly synchronized activity. It is this regime that is typically used to model neural dynamics.

Here, resting state activity is simulated as the cortical response due to unstructured white noise  $a_{ne} I$ , where  $I$  is the nonspecific subcortical current. As the system of equations exhibit emergent chaotic behavior, it is only nescessary to include an initial condition for the noise across all nodes to reproduce this behavior.

The model parameters are listed in Table XXX, and is computationally integrated using the Brain Connectitiv toolkit (REF) in MATLAB.

-> inputs to BOLD forward model

**The Hopf bifurcation model.** Lastly, instead of applying a specific biophysical model we can aim to reproduce three key types of dynamics observed in vivo - oscillations, noise and the combination - noisy oscillations. This model uses the supercritical Hopf bifurcation oscillator - which is a normal form to model the observed dynamics and approximates the behaviour of a large array of coupled dynamical systems and biophysically realstic models (Robinson, Freyer, Break-spear). The dynamical system describes dynamics for over two variables  $x_i, y_i$  per node  $i$  through a series of coupled stochastic differential equations described as:

$$\frac{dx_i}{dt} = [a - x_i^2 - y_i^2] x_i - \omega_i y_i \dots \quad (15)$$

$$\dots + G \sum_j C_{ij} (x_i - x_j) \beta \eta_i(t), \quad (16)$$

$$\frac{dy_i}{dt} = [a - x_i^2 - y_i^2] y_i - \omega_i x_i \dots \quad (17)$$

$$\dots + G \sum_j C_{ij} (y_i - y_j) \beta \eta_i(t), \quad (18)$$

where  $a$  is the bifurcation parameter that at the nodel level tunes the system to be within three regimes. At the individual nodel level without coupling ( $G = 0$ ), if  $a > 0$  the system is in an oscillatory regime with frequency  $\omega_i$ , and if  $a <= 0$  the system lies on a fixed point and does. When coupling between nodes is introduced with multplicative noise Gaussian noise  $\eta(t)$  (with standard deviation  $\beta$ ) in the term  $G \sum_j C_{ij} (y_i - y_j) \beta \eta_i(t)$  the dynamics of the system changes its characteristics with the bifurcation parameter  $a$ . When  $a < 0$  the dynamical system now exhibits noisy dynamics, but when around  $a = 0$  the system exhibits noisy oscillations, and when  $a > 0$  the system exhibits the oscillatory behaviour. The frequency  $\omega_i$  is estimated from resting state data itself by calculating the peak frequency within the narrow frequency band from 0.04 to 0.07 Hz.

This model requires two additional parameters to be fit: the global coupling parameter  $G$ , and the bifurcation parameter  $a$ . Firstly, as in the balanced E-I model,  $G$  is a hyperparameter that is optimized for best fit on the similarity of the FC matrix and the dynamic FC (as described in the proceeding sections). Following this, the bifucation parameter  $a$  is then fit according to similar principles to further improve fits. The

dynamical equations are solved with MATLAB 2019, using an Euler Muryami integration scheme.

**Imposing Heterogeneity.** The presented models impose uniform node parameters, and although they provide moderate predictive power on static FC, they often lack in the predictive power on dynamic FC measures. To improve the overall fitting on both dynamic and static FC, we can increase the degrees of freedom by imposing heterogeneity on the node parameters. This variation can be understood in terms of dynamics and the underlying biology. Dynamically, when nodes are parameterized with uniform parameters the dynamics are shaped by the emergent behaviour from network interactions. Variations of parameters can increase the dynamic range of the system. Biologically, uniform node parameters approximate neurophysiology, as local neuronal connectivity, lamination of cortex, and neuronal types vary throughout cortex and subcortex (REFS). In terms of observed dynamics, heterogeneity can change local dynamics causing - but not limited to - changes in the autocorrelation, excited frequencies, and the ratio between noise and oscillations.

However, imposing this heterogeneity requires either some a priori knowledge such as the myelin markers as in (Dermitas et al.) or by optimizing node parameters to improve model fits. Here, we vary node parameters to optimize model estimates in functional connectivity similarity and dynamic functional connectivity (see below). Due to the ease of integration of the Hopf model, we impose heterogeneity in the model by varying the bifurcation parameter  $a$  to be described at the node level yielding:

$$\begin{aligned} \frac{dx_i}{dt} &= [a_i - x_i^2 - y_i^2]x_i - \omega_i y_i \dots \\ &\dots + G \sum_j C_{ij}(x_i - x_j)\beta\eta_i(t), \end{aligned} \quad (19)$$

$$\begin{aligned} \frac{dy_i}{dt} &= [a_i - x_i^2 - y_i^2]y_i - \omega_i x_i \dots \\ &\dots + G \sum_j C_{ij}(y_i - y_j)\beta\eta_i(t). \end{aligned} \quad (20)$$

The model is estimated following Deco et al, where the model is first fit by optimizing model fits of FC, and FCD (described below) with respect to  $G$ . Following this,  $a_i$  is optimized with a greedy search algorithm to optimize FCD. (insert some details here?)

**Assessing model accuracy.** The resulting neural dynamics from both the neural mass model and the balanced EI model are translated to BOLD activity via a convolution model typically used in BOLD fMRI studies (REF Boynton). As the Hopf bifurcation model simulates dynamics at the time scale of BOLD fMRI, it does not need a forward model and the dynamics of  $x_j$  are the dynamics of the BOLD fMRI fluctuations. Assessing the accuracy of model simulations is achieved by how well the model can fit experimental rsfMRI. The comparison metrics to quantify model fit can be split up into two different types of metrics those that are static and dynamic.

++ Might have to say in each model it was run for XX mins and BOLD data was YY. +++

The most straightforward static comparison metrics is by using the functional connectivity matrix. Namely, once the model has been estimated pearson correlations between each node is calculated (as in the experimental data). As the functional connectivity matrix is symmetric, we compare how well the upper triangle of the model FC matrix correlates the upper triangle of the experimental FC described by the following similarity measure (fix up eq):

$$FC_s = \text{corr}(\text{arctanh}(\text{FC}^{\text{exp}}), \text{arctanh}(\text{FC}^{\text{sim}})). \quad (21)$$

This metric is the initial target of parameter optimizations as it is a necessary, but not sufficient, condition that models need for plausibility. In all the models presented the choice of the hyperparameter  $G$ , that scales the overall coupling of the connections, is varied to maximize  $FC_s$ .

Models with a sufficiently high  $FC_s$  can however, patterns simulate resting state fluctuations that are inconsistent with the observed dynamics. For this reason, measures of the fluctuations were imposed to add additional constraints to find models. Here, we focus on a recent measure the dynamic functional connectivity statistic (FCD).

Firstly, the dynamic functional connectivity captures the variation of FC over time. The FCD is achieved by calculating the FC over a small time window of length LL, and this window then slides over time to cover YY minutes. At each FC calculation, the average FC is calculated and zzz. Then the distribution of this is calculated over a single instance in the modelling or at a group level. The comparison metric is not with any single instance of the FC, but over all time combinations to compare the distributions of the FC. The degree of similarity can be measured by using the Kolmogorov-Smirnov statistic - a measure that is regularly used to compare distributions. This KS statistic measures the “distance” between two distributions, and a model that captures the same fluctuations will be minimized on this metric.

In the heterogeneous models, parameter variations at the node level can alter the dynamic fluctuations and thus these models are optimized to minimize the KS-statistic (FCD). These are done via a greedy search algorithm, where changes in parameters are defined following linear perturbations to minimize the KS statistic.

## Results

The results are structured as follows. Firstly, we investigate the spatiotemporal characteristics of the data that need to be modelled. We then characterize the spatiotemporal characteristics of the models themselves, and compare the gross features of the models with data. Following this, we describe the accuracy of the fits to data in the static and in the dynamic regime. Lastly, we show that we can improve the models by employing heterogeneity in the model populations and in the estimates of effective functional connectivity.

**Wide spread deflections in rsfMRI data.** To understand the effects of artefacts on modelling, it is important to char-

acterize the issues within rsfMRI. Here, we reiterate the important aspects within rsfMRI and why they are important to modelling resting state fMRI.

Firstly, an important technique to analyze the quality of resting state fMRI scans is to visualize the spatiotemporal time series of scans. As shown in Figure 1C, (MPP looks pretty similar, might include a noisier subject..) that following minimal preprocessing (MPP) a “low-motion” subject from the UCLA cohort (sub-10274) contains a wealth of wide-spread signals that are times tied to motion events as captured by the mean framewise displacement (FD) - highlighted by the blue rectangles. Additional wide-spread signals have also been tied to physiological events such as respiration (23, 25) or heart rate variability (26). A robust de-noising method - ICA-AROMA with regression of white and CSF signals (+2P) mitigates some of these events however often with these algorithms that use spatial ICA we are left with residual WSDs (23, 27) which can be appreciated in Fig. 1D. The link between these WSDs with physiology and motion thus treats these characterises these particular WSDs as noise. The effect of this WSD is expressed in the functional connectivity matrix in Fig 1G, where the WSD causes a FC matrix that is positively correlated for almost all edges. This is an important issue because if the FC matrix is used to compare between groups, then large motion or physiology drives the changes in the edges of the FC matrix rather than underlying neuronal processes. For these reasons, further de-noising is often employed to rid rsfMRI of these artefactual signals. As described in the methods GMR is regularly used to rid rsfMRI of these influences, and as seen in Fig 1E, it can help mitigate these effects with the side effect of introducing negative correlations due to this zero-centering (28, 29) which can be appreciated in Fig 1H and Fig 2H. Using the mean of all voxels to remove WSDs can be problematic if the WSD is made of components that exist in multiple phases such as the subject in Fig. 2 where the common underlying WSD is expressed in two clear phases - i.e. the top half has the opposite sign of the bottom half. As can be appreciated in Fig. 2D vs Fig. 2E, GMR does not remove this WSD adequately, leaving behind a spatiotemporal time series that still contains artefactual WSD. This characterization of the types of WSDs is explained in (12) and can be thought to be of three types: weak (not shown here), single-phase, and biphasic.

For these reasons, a new technique - DiCER - was developed to targets these weak diffuse signals (12) in order to remove WSDs. On application of DiCER to the ICA-AROMA+2P output form all subjects, the carpet plots in Figures 1F and 2F show the reduction of WSDs, whilst revealing FC matrices in Figures 1 I and 2 I that have structure without zero centering the functional connectivity matrix. We note that undergoing network discovery, DiCER appears to improve statistical sensitivity of neuronal components - or at worst - on par with GMR (12). These type of WSDs are present across the three datasets described, and the removal of the WSDs by DiCER or GMR generally improves QC-FC measures (not sure how much detail, perhaps will show QC-FC for UCLA,BZ and HCP).

**Wide spread deflections in models of rsfMRI.** The above results illustrate that the nature of coherent structures are largely seen as artefactual and the presence of these structures are removed with varying degrees of de-noising. The varying degrees of WSDs are important to biophysical models of resting state fMRI, as the models not only have to capture the overall functional connectivity but the typical dynamics within data. As described in the methods, a key feature of all biophysical models is the global coupling parameter  $G$ , that changes the dynamics of the models from un-coupled dynamical nodes ( $G = 0$ ) through to completely synchronized dynamics ( $G > 4$  in the models considered here). Therefore, the tuning of the model and the dynamic regime will depend on the quality of the data with regards to the level of WSDs. This can be appreciated by analyzing the WSDs in the biophysical predictions in a similar fashion to the experimental data.

Firstly, for the Balanced Excitation Inhibition model Fig. 3 A shows that varying the global coupling parameter  $G$  largely changes the dynamics of the model. If we compare the carpet plots of varying levels of the coupling parameter  $G$  we see visually that the level of WSDs increases as  $G$  increases and is reflected in the global structure in the functional connectivity matrices in Fig. 3 B. The level of WSDs can be quantified by using heuristics, here we use the variance explained by the first PC (VE1) or the global mean of all correlations in the FC matrix (here we use the absolute value of the FC matrix) (GFC). As shown in Figs 3 C, and 3 D we can see that like in the carpet plots and the FC matrix, VE1 and GCF increases as  $G$  increases. When comparing these measures to subject 10274 in the UCLA data we find that the level of synchrony needed to match the data depends on the level of WSDs within the data that are dependent on the preprocessing pipeline. Overall, these features are shown in the neural mass model in Fig. 3 F-I as well as the Hopf bifurcation model in Fig. 3 J-M. Where the transition from uncoupled noisy nodes to a synchronous pattern increases gradually in the Balanced EI model (Fig. 3 C,D) and in the Hopf bifurcation model (3 L,M), and is a phase transition in the Neural mass model (Fig. 3 H,I).

The above results indicate that data with WSDs requires models to be biased toward the synchronized regime, whereas data with reduced WSDs push data to the unsynchronized regime (i.e. lower  $G$ ). We stress that the data used for comparison comes from the same subject here but undergoing different degrees of de-noising. We can explore this issue in the two regimes. Firstly, models within the synchronized regime appear to have a globally coherent signal visually expressed by the large vertical stripes in Figs 3 A,F,J with  $G = 3, 3.25, 2 - 8$  respectively. If we were to model this behaviour explicitly, we first note that in all three models the local dynamics at node  $i$  are modulated by the influences owing to the sum (or mean) of the neighbouring nodes weighted by  $C$  i.e. by a general factor

$$G \sum_j C_{ij} f_j(t), \quad (22)$$

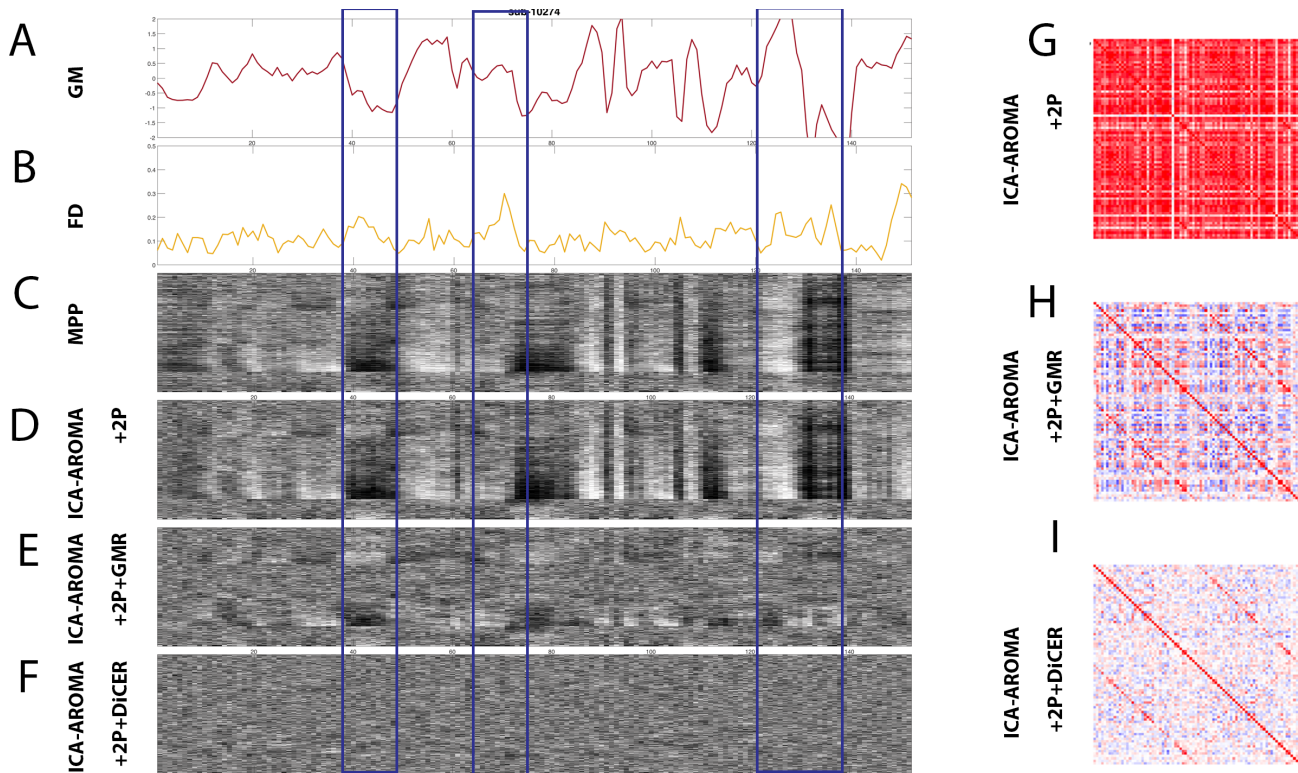


**Fig. 1.** Wide spread signals in a single-phase WSD - subject sub-10274 in the UCLA cohort. The first two signals express the A. signal averaged across all gray matter and B. framewise displacement (FD). The following four panels are carpet plots for the C. Minimal preprocessing pipeline (MPP), D. ICA-AROMA with white matter and CSF regression (+2P) pipeline (following MPP) E. Grey matter regression (GMR) following ICA-AROMA+2P pipeline, and F. Diffuse cluster estimation and regression (DiCER) following ICA-AROMA+2P pipeline. The last three panels show the corresponding functional connectivity matrices for G. ICA-AROMA+2P, H. ICA-AROMA+2P+GMR, and I. ICA-AROMA+2P+DiCER.

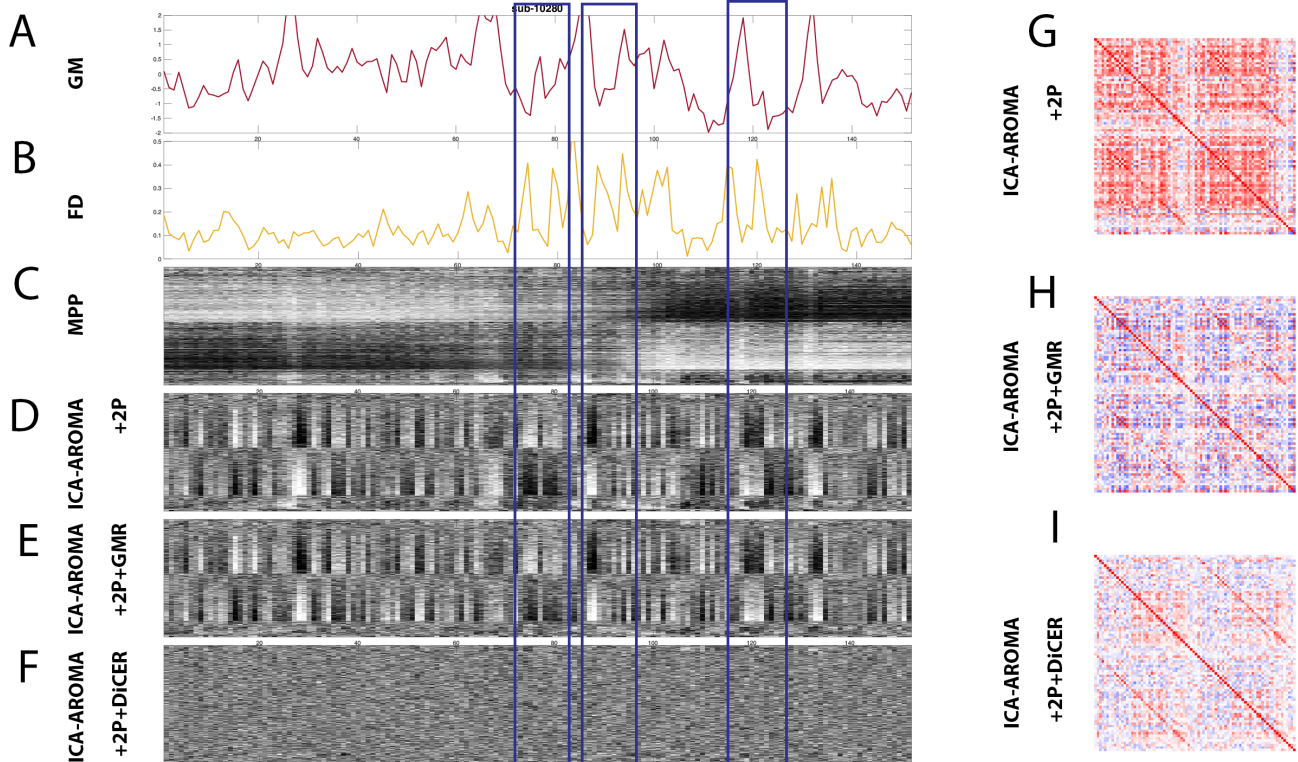


**Fig. 2.** Wide spread signals within a biphasic subject - sub-10724 in the UCLA cohort. The first two signals express the A. signal averaged across all gray matter and B. framewise displacement (FD). The following four panels are carpet plots for the C. Minimal preprocessing pipeline (MPP), D. ICA-AROMA with white matter and CSF regression (+2P) pipeline (following MPP) E. Grey matter regression (GMR) following ICA-AROMA+2P pipeline, and F. Diffuse cluster estimation and regression (DiCER) following ICA-AROMA+2P pipeline. The last three panels show the corresponding functional connectivity matrices for G. ICA-AROMA+2P, H. ICA-AROMA+2P+GMR, and I. ICA-AROMA+2P+DiCER.

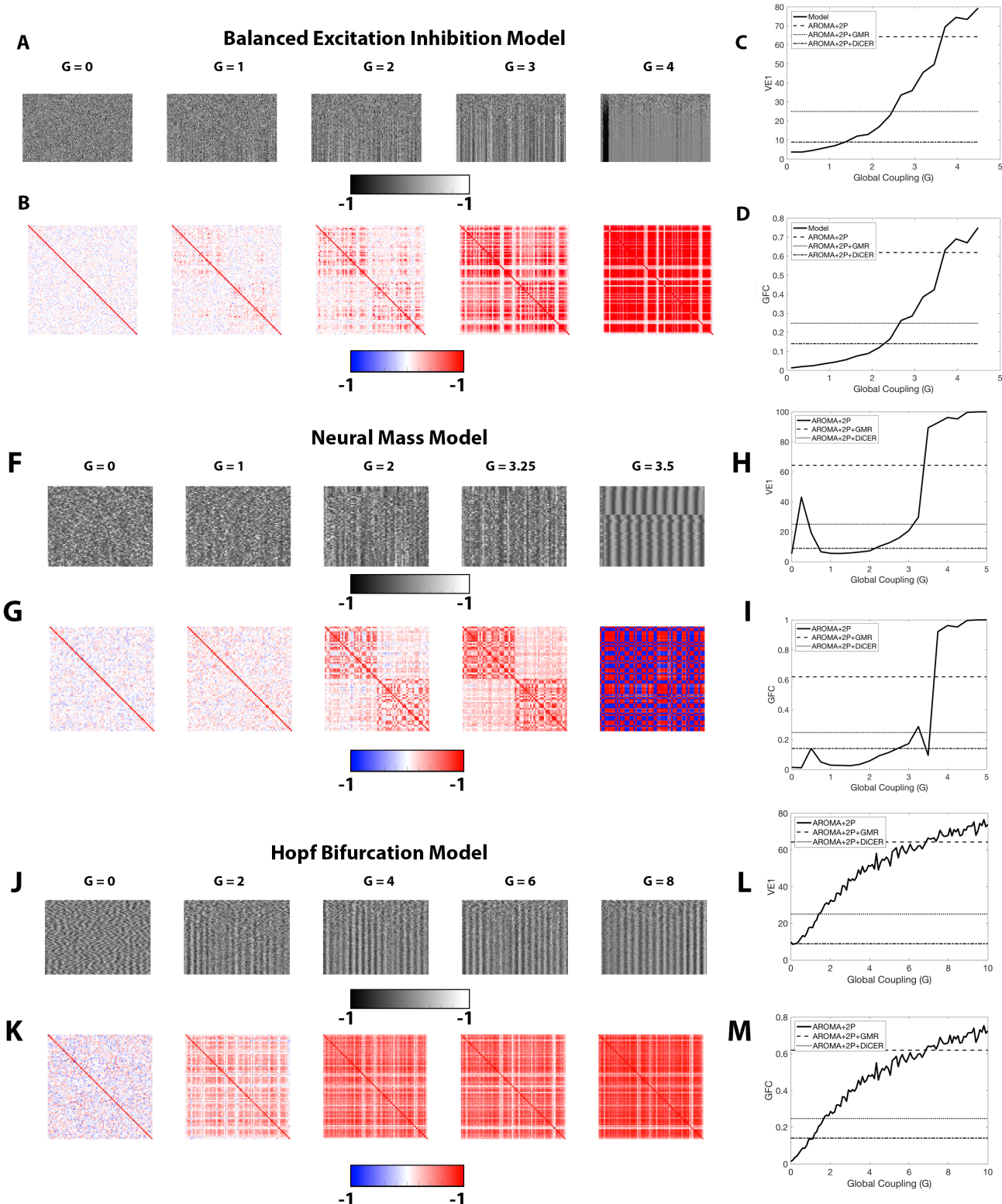


**Fig. 3.** Wide spread deflections in biophysical models of resting state fMRI. In the three models presented here we show spatiotemporal carpet plots and functional connectivity matrices as a function of the global coupling parameter  $G$  in (A,B), (F,G) and (J,K) for the balanced EI, neural mass and Hopf bifurcation models respectively. Quantitative metrics of variance explained by the first PC (VE1) and global functional connectivity are shown in (C,D), (H,I), and (L,M) for the balanced EI, neural mass and Hopf bifurcation models respectively. In the metrics (i.e. the panels on the right) we calculated these values for subject 10274 under three different preprocessing pipelines.

where  $f_j(t)$  is a generic function that describes some output node  $j$  expressed to node  $i$ . In most models  $f_j(t)$  are the dy-

namics of excitatory population at node  $j$  projected to node  $i$ . Thus, if all nodes shared a common signal  $\sigma(t)$  the dynam-

ics at node  $i$  will be modulated by this common factor and a local Gaussian noise term  $N(0, 1)$  (owing to noisy inputs in all the three models) expressed as:

$$z_i(t) = \alpha N(0, 1) + G \sum_j C_{ij} \sigma(t), \quad (23)$$

$$= \alpha N(0, 1) + GD_i \sigma(t), \quad (24)$$

where  $D_i$  is the node degree, and  $\alpha$  determines the strength of the noise term which we set at  $\alpha = 1/2$  when considering z-scored common signals  $\sigma(t)$ . Here, we describe neural dynamics however, since this is a linear process then we replace  $z_i(t)$  with the estimate of the BOLD signal  $B_i(t)$  if  $\sigma(t)$  is within the same time scales. When we use the common signal as the mean signal of sub-10274, this noisy degree model in Fig 4 can reproduce carpet plots and FC matrices similar to the preprocessing pipeline ICA-AROMA+2P with  $G = 4$ . Therefore, a model of the global signal modulated by node degree is roughly equivalent to highly synchronized models of rsfMRI, and is well correlated to dynamics of the balanced to the Balanced Excitation Inhibition model ( $r = 0.99$ ). (think about how this fits in..)

In the weakly synchronized regime, there are fewer WSDs and there is closer match with data undergoing GSR or DiCER. However, within the experimental fMRI literature, a key argument against the use of GMR is that it may remove neurally related WSDs. Here, the presented models simulate globally coherent neuronal fluctuations, thus a key question is what remains post GMR. Following GMR, we see three types of artefactual effects in the three presented models in Fig. 5. For low  $G$ , WSDs are removed lowering VE1 and GFC (we exclude the noisy degree model as by construction, as all of the non-noisy signal is removed post GMR). This effect is present however, for all  $G$  for the Hopf bifurcation model. Secondly, When there is a globally coherent signal that is delayed between nodes - such as those imposed by a travelling wave (Roberts et al.) - the mean signal can does not capture the WSD such as in the neural mass model for  $G = 3.5$  as in Fig. 3 F thus leaving WSDs post GMR in Figure. 5 E,F. In all models and global parameter variations, only the neural mass model for  $G = 2 - 3$  and the balanced EI model for  $G = 2, 4$  leaves residual structure in the FC matrix, indicating residual modulations above globally coherent ones. These are visual comparisons and provide indications of the artefacts and FC matrix structure. Quantitative comparisons with rsfMRI are described in the next section.

**WSDs affect model fits.** With a characterization of the wide spread deflections in rsfMRI data and modelling, we can now explore how well these features correspond to quantitative model fits. In Figure 6 we show the results of fitting functional connectivity similarity in the four models presented over three de-noising pipelines in the UCLA cohort. We note in all four models, model fits with regard to FC similarity are maximised with ICA-AROMA, with a global coupling factor that corresponds to model predictions with large global synchrony (as described above). This globally coherent feature is emphasized when comparing the FC of

the model at optimal fits with the group average FC matrix in Fig. 6 E, i.e. regions are highly correlated to one another. The slight exception is the neural mass model, that has a lower overall fit. It is worth noting that the noisy degree model on data with large WSDs fits well with this analysis metric and only contains one parameter ( $G$ ).

As described above, GMR applied to rsfMRI models can reduce coherent signals and thus an important question remains - what neuronal information is left post GMR and how well does this fit rsfMRI that has undergone a reduction of WSDs with GMR or DiCER. When comparing rsfMRI models that have undergone GMR, we find that the performance of three of the presented models drop from 0.55 to 0.35 in the Balanced EI model, from 0.6 to 0.2 in the Hopf Bifurcation model, and 0.56 to 0.1 in the Noisy degree model to data that has undergone GMR or DiCER. In these models, WSDs dominate the dynamics thus their removal leaves residual dynamics that is less compatible with rsfMRI that has been de-noised past ICA-AROMA, which can be appreciated in the FC matrices in Figs. 6 F,G. Note that these results hold if the focus was restricted to unihemispheric dynamics. On the other hand, the dynamics in the neural mass model are weakly synchronized for  $G < 3.25$  and thus upon GMR the dynamics and the functional connectivity structure is unchanged - albeit shifted toward the negative, and the fitting of this model with the data is relatively unchanged, however poor (0.3).

Beyond static measures, dynamic measures of functional connectivity provide additional constraints on the models, thus the models can also be tested in terms of how well their dynamics match data. Here, we use phase-lagged coherence (what else do you call it Gustavo..) which, as stated in the methods, calculates the phase difference between all nodes for data within a window and correlates this with shifted versions of this window, as indicated in Fig. 7 A for subject 10274 in the UCLA cohort. The phase-lagged coherence at  $\phi_{ij}$  represents the difference between the synchronization level of the entire network at a time shift  $\tau_i$  with a time shift  $\tau_j$ . Structure within  $\phi_{ij}$  at different time shifts is usually interpreted as the dynamics of the persistence and decay of states of the network (i.e. at clusters we have similar coherence structure). What can be appreciated is that the structure of  $\phi_{ij}$  is reduced once the data has been de-noised in GMR or with DiCER - i.e. the persistence of states are reduced, leaving only the diagonal as the main structure. Since the structure of  $\phi_{ij}$  is dependent on a particular instance of the rsfMRI or model simulation, we instead focus on the distribution of the upper triangle of  $\phi_{ij}$  instead as this determines the overall nature of these fluctuations. Figure 7 B indicates the aggregated histogram for all subjects. Here we emphasize that the fluctuations are correlated over time at different degrees - indicated by the spreading of the distribution from 0 (i.e. uncorrelated structure over time) to 1 (instances where the structure is preserved over time shifts). As the data is de-noised there is a shift to 0 indicating that this apparent time-lagged structure is largely dependent on the level of WSDs, thus WSDs bias these measures as well. When com-

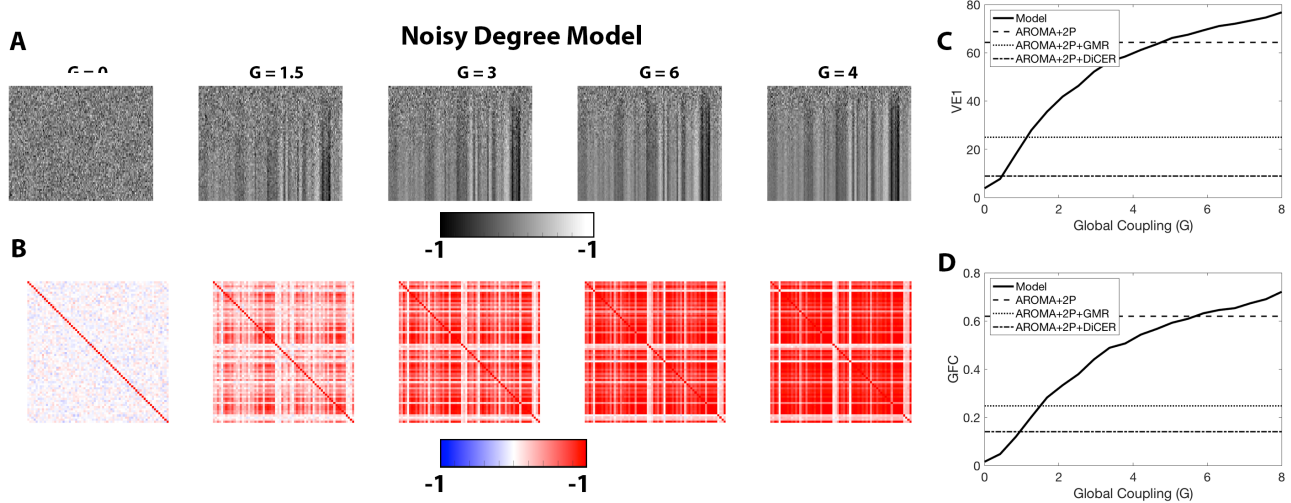


**Fig. 4.** Wide spread deflections in the noisy degree model for resting state fMRI. Here we show spatiotemporal carpet plots in A and functional connectivity matrices as a function of the global coupling parameter  $G$  in B. Quantitative metrics of variance explained by the first PC (VE1) are shown in C and global functional connectivity are shown in D. In the metrics (i.e. the C, and D) we calculated these values for subject 10274 under three different preprocessing pipelines.

paring the phase-lagged structure and histograms applied to the optimal models in the balanced EI model - i.e. the optimal model for balanced EI with ICA-AROMA and the optimal models for balanced EI+GSR for comparisons to ICA-AROMA+GSR and ICA-AROMA+DiCER. The shift toward 0 in the histogram is also present in the models that seem to generally match the histograms in the group data. To compare this quantitatively, a Komologrov-Smirnoff test (KS) is used to compare the histograms for similarity. The KS statistic from this test is called the Functional Connectivity Dynamic (FCD) and a small FCD implies a closer fit, and a large FCD (close to 1) implies a divergent fit.

In Figure 8 FCD calculated for the four presented models in a similar fashion to Figs. 6. Similar to the FC results, as we vary the level of synchrony in the models by varying  $G$ , the fits of dynamic properties vary and their associated fits to different denoising pipelines. However, unlike the fits for the FC matrix, in all models there exists a minimum for fitting the dynamics of the model to data, and this minimum is the same for all the model associated comparsions to the three denoising methods i.e. a KS statistic  $\approx 0.05$ . It is noted that for each model, the minimum of the KS statistic occurs at a  $G$  that is different to the maximum similarity of the FC matrix, for example in the ICA-AROMA pipeline the maximum similarity for the balanced EI model occurs at  $G = 4.5$ , however in terms of FCD this occurs at  $G = 2.8$ . This divergence means that while the FC matrix can be reproduced, the fluctuations are not at odds with the fluctuations present in the data. We note that since the noisy degree model exhibits similar FCD performance to the other three other models, FCD is likely a feature of the time series i.e. properties such as autocorrelation as the noisy degree model is merely a global signal model. Thus optimization over FCD may just guide the time scale of general fluctuations and not an accurate representation of change of brain states.

**Using heterogeneity to improve fits to data with low WSDs.** Here we explore models that introduce heterogeneity that additionally focus on dynamic functional connectivity. Here, we introduce heterogeneity in two forms: at the node level and at the edge level (i.e. optimizing the structural connectivity matrix). In both forms heterogeneity is imposed by finding optimal functional connectivity at a given  $G$ , then modulating parameters (at the node or edge level) to minimise the FCD. In our previous section we showed that if models were fit to data with large WSDs, such as those present in the ICA-AROMA scheme, then models will be biased to have WSDs. Thus our heterogenous variations are imposed on data that has reduced WSDs. As both heterogenous variations require optimzation, these models are performed with the Hopf Bifcaktion model for computational efficiency over the other models.

Firstly for the heterogenous node parameters, we use the approach in Deco et al. 2018, where for a given coupling  $G$ , the parameter  $a_i$  for node  $i$  in equations 19&20 is varied in a way to minimize FCD. This is achieved in a greedy algorithm, where each node  $i$  the bifurcation parameter  $a_i$  increased or decreased at each iteration by a factor of XXX depending on the phase difference. This greedy algorithm converges and the result of the algorithm finds the lowest FCD for a given parameter  $G$ . Below in Figure 9 we see that although we have improvement on FC and FCD, the measures are of low fit. In addition, this improvement was achieved by increasing the degrees of freedom by modifying 88 parameters for which additional complexity has been added for low improvement of fit.

Secondly, an additional heterogeneity was used estimate the directed effective connectivity, that is to adjust the edge weights within the structural connecivity matrix. This process invovled a greedy search algorithm to improve the fits of the FCD while maintaining a homogenous hopf bifurcation

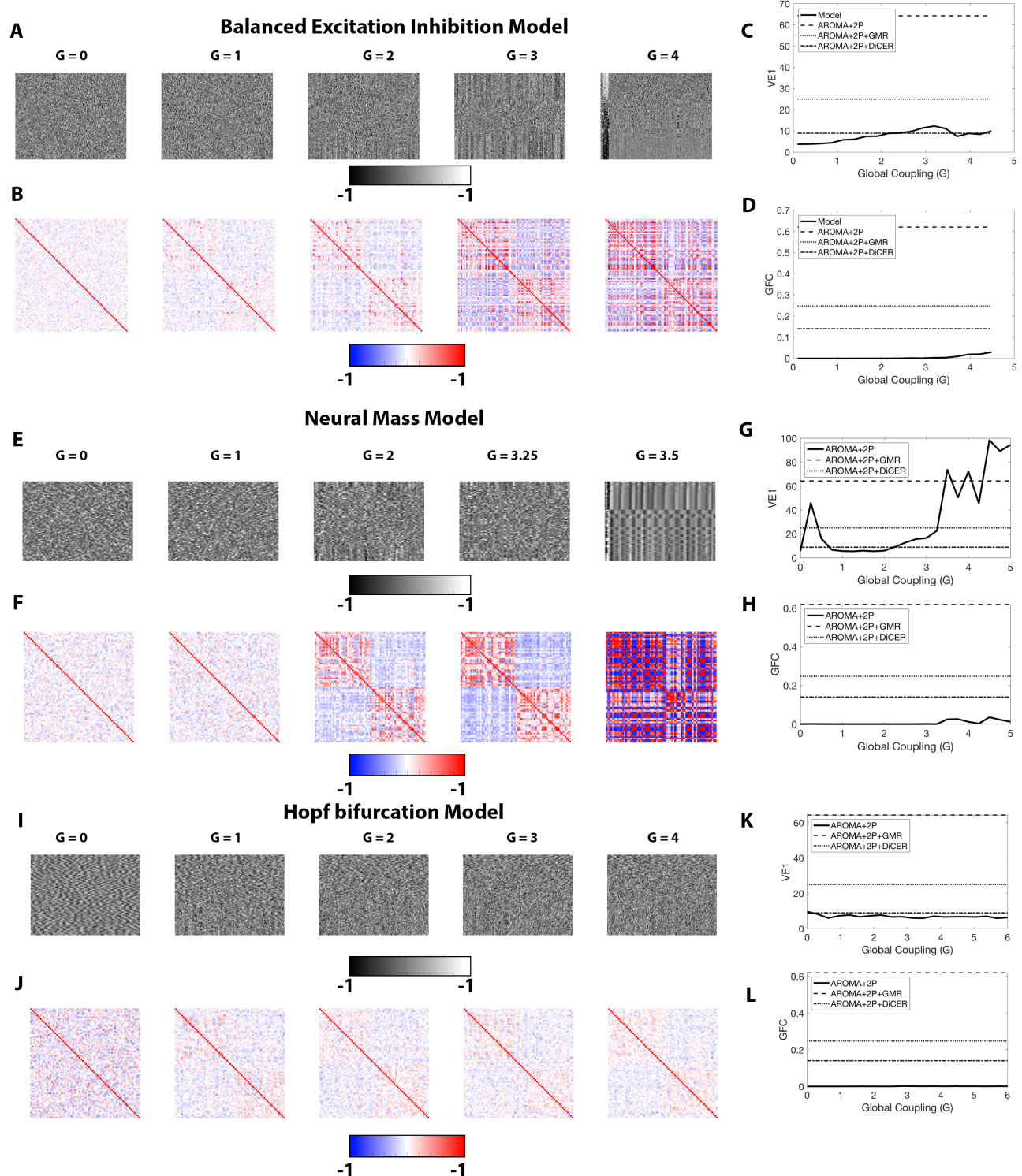
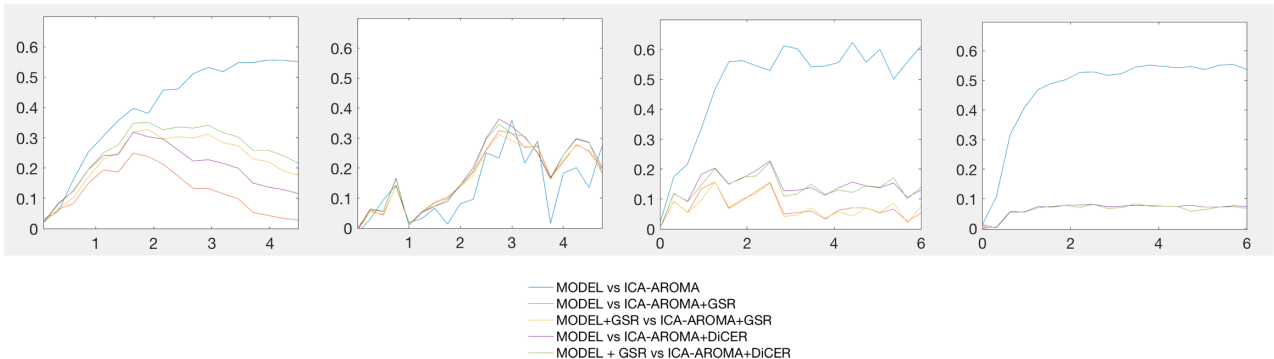


**Fig. 5.** What is left post GMR in biophysical models of resting state fMRI. In the three models presented here we show spatiotemporal carpet plots and functional connectivity matrices following GMR as a function of the global coupling parameter  $G$  in (A,B), (F,G) and (J,K) for the balanced EI, neural mass and Hopf bifurcation models respectively. Quantitative metrics of variance explained by the first PC (VE1) and global functional connectivity are shown in (C,D), (H,I), and (L,M) for the balanced EI, neural mass and Hopf bifurcation models respectively. In the metrics (i.e. the panels on the right) we calculated these values for subject 10274 under three different preprocessing pipelines.

model, the steps are as follows.... (maybe include the steps on how ANEC is actually formed).

This adjustment is on all the non-zero edges in the structural connectivity matrix, and can involve a large number of edges

**A** Balanced EI model    **B** Neural Mass Model    **C** Hopf Model    **D** Noisy degree Model



Best fitting FC matrices per model vs Data

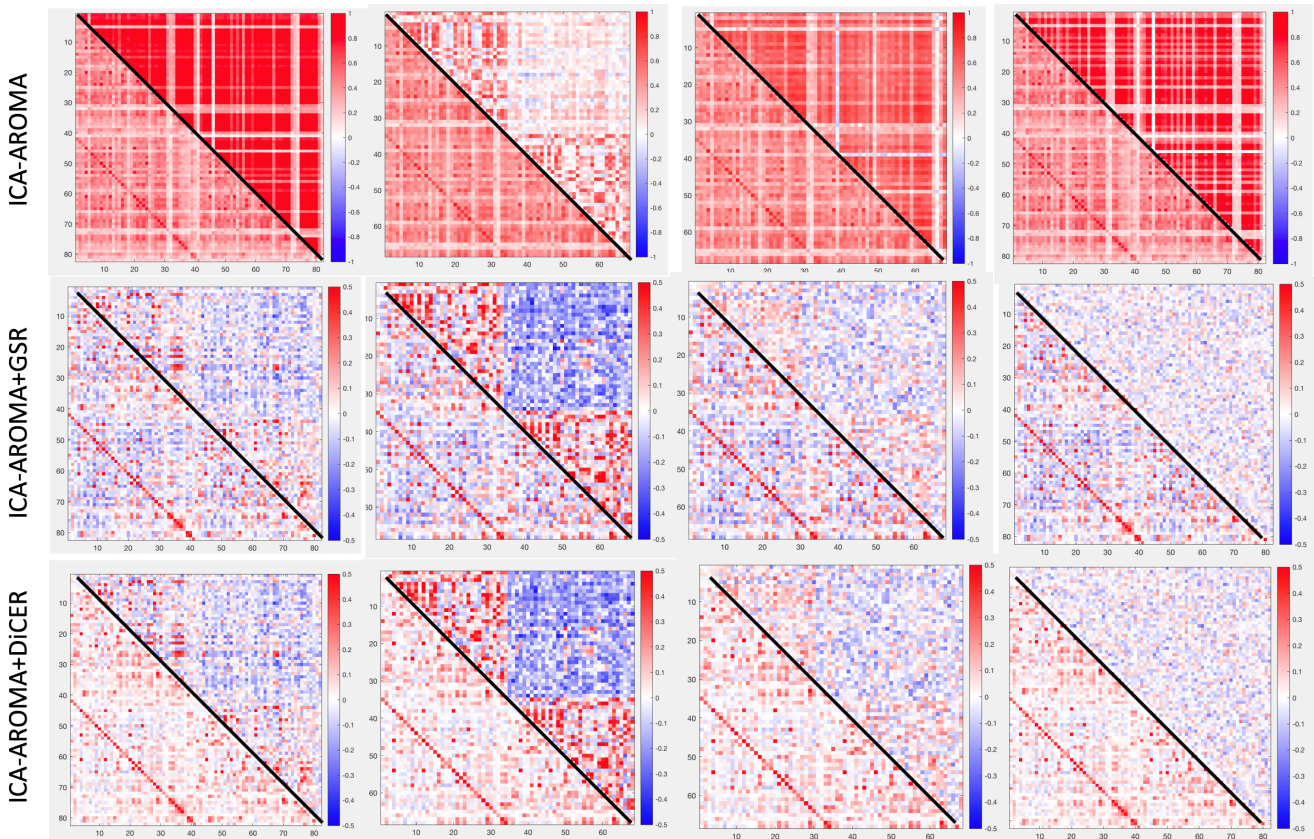


**Fig. 6.** Fitting of biophysical models to data. For the balanced EI model in A, the top panel shows the FC similarity of the model vs a group-averaged functional connectivity matrix under three different pipelines. The similarity is compared with the model vs ICA-AROMA, model vs ICA-AROMA+GMR, model+GMR vs ICA-AROMA+GMR, model vs ICA-AROMA+DICER and model+GMR vs ICA-AROMA+DICER. Below this comparison, we show the optimal functional connectivity matrix when using the model vs ICA-AROMA, then the model+GMR vs ICA-AROMA+GMR and finally model+GMR vs ICA-AROMA+DICER. In the three bottom plots the upper triangle is the model fits, and the lower triangle is the FC from the optimized fit. This is repeated for the Neural mass model in B, the Hopf bifurcation model in C and the noisy degree model in D.

to be modified. In order to help account or over-fitting, we fit this optimization on 85% of the subjects and then apply this optimization on the remaining 25%. In Figure 10 we find that the functional connectivity as well as the dynamic functional connectivity is improve when using data without WSDs. Although this shows a dramatic improvement in both FC and FCD, we note however that we have allowed many of the edges of the structural connectivity matrix to vary leading to an explosion of  $(88 * 88 - 88)/2$  parameters.

Another avenue is to explore the following: 1. Take the

T1/T2 Ratio and use this as an axis to vary the bifurcation parameter,  $a = a_0 + \alpha T_1/T_2$ . 2. Another way to do this is to take the T1/T2 ratio and use this to add additional stuff to the connectivity matrix i.e.  $C = C_0 + \alpha T$ , where  $T_{ij} = 1 - |(T_1/T_2)_i - (T_1/T_2)_j|$ , thus we add connections to populations that are on the same level of the cortical hierarchy.

+++Or just talk about how additional measures are needed, here we show as a proof of principle extra information is needed and can be done via heterogeneity – a positive spin

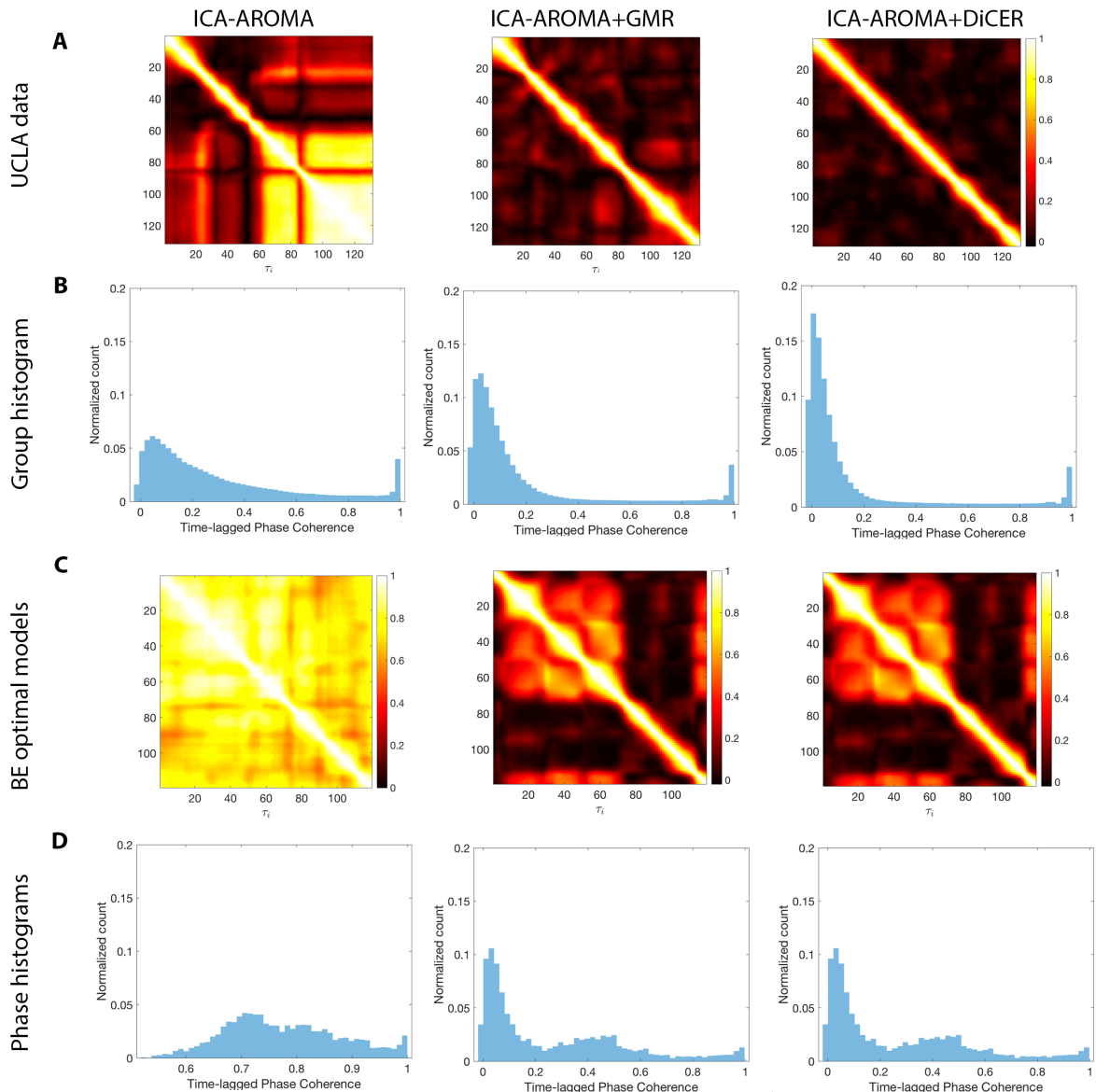


**Fig. 7.** Phase-lagged dynamic connectivity. A  $\phi_{ij}$  calculated for ICA-AROMA, ICA-AROMA+GMR and ICA-AROMA+DiCER. B The aggregated histogram across all 100 subjects in the UCLA cohort under three different pipelines. C  $\phi_{ij}$  calculated for optimal models for the ICA-AROMA pipeline, and for the ICA-AROMA+GMR and ICA-AROMA+DiCER pipelines where the models have undergone GMR as well. Below in D are the associated histograms derived from C.

that it can be done, we just need to find heterogeneity.

## Discussion

**QC evaluation of models is needed.** Talk about the types of QC that we brought up and how they are needed.

**WSDs in data bias models.** Talk about how WSDs in data show global patterns, although they may be neural they flood models i.e. models end up just being models of the global signal.

**Evidence against using data for modelling without some denoising.** Need to discuss that a common reason not to use GMR (or even other WSD reducing types of analysis) is that it will impact neuronally driven WSDs - a feature in

many models (as seen above). However models may just be fitting this and nothing else if they are not careful.

**The Noisy degree model as a null model.** Talk here, that if you are going to use ICA-AROMA, or any other data with WSDs they have to beat the noisy degree model.

**Heterogeneity is the way to go, but there are limitations.**

**Study limitations.**

## Notes

+ Parcellation discussion increase + Need to finish HCP and BZ fitting + Need to redo on HCP 360 + 20 SC parcellation

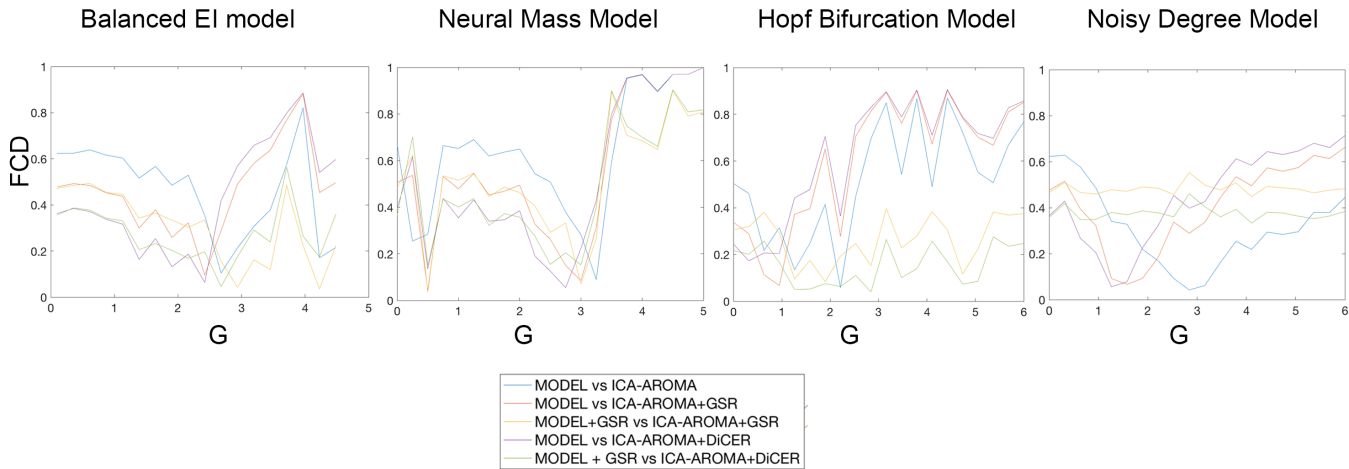


**Fig. 8.** FCD comparisons for the model simulations across three pipelines with the following combinations: model vs ICA-AROMA, model vs ICA-AROMA+GMR, model+GMR vs ICA-AROMA+GMR, model vs ICA-AROMA+DiCER and model+GMR vs ICA-AROMA+DiCER. This is calculated for the Balanced EI model in A, the neural mass model in B, the Hopf bifurcation model in C and the noisy degree model in D.

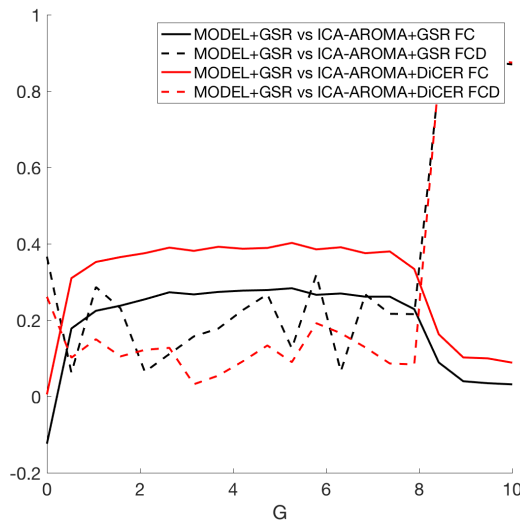


**Fig. 9.** Hopf heterogenous, showing the FC and the FCD when comparing to ICA-AROMA+GMR and ICA-AROMA+DiCER.

(taking some time) + Need to consider last bits of the analysis, compare with custom 200?

## Acknowledgements

### ACKNOWLEDGEMENTS

AF was supported by the Australian Research Council (ID: FT130100589), National Health and Medical Research Council (NHMRC; ID: 1104580), and the Sylvia and Charles VierTEL Charitable Foundation. The authors thank Stuart Heitmann for support of the Brain connectivity toolbox, and Christopher Honey and Olaf Sporns for sharing code.

## Bibliography

- M. D. Fox, A. Z. Snyder, J. L. Vincent, et al. The human brain is intrinsically organized into dynamic, anticorrelated functional networks. *Proc. Natl. Acad. Sci. USA* **102**, 9673 (2005).
- S. M. Smith, P. T. Fox, K. L. Miller, et al. Correspondence of the brain's functional architecture during activation and rest. *Proceedings of the National Academy of Sciences* **106**, 13040 (2009).
- C. F. Beckmann and S. M. Smith. Probabilistic independent component analysis for functional magnetic resonance imaging. *IEEE transactions on medical imaging* **23**, 137 (2004).
- E. S. Finn, X. Shen, D. Scheinost, et al. Functional connectome fingerprinting: identifying individuals using patterns of brain connectivity. *Nature neuroscience* **18**, 1664 (2015).
- E. Amico and J. Goñi. The quest for identifiability in human functional connectomes. *Scientific reports* **8**, 8254 (2018).
- J. Li, R. Kong, R. Liegeois, et al. Global signal regression strengthens association between resting-state functional connectivity and behavior. *BioRxiv* p. 548644 (2019).
- R. Ciric, D. H. Wolf, J. D. Power, et al. Benchmarking of participant-level confound regression strategies for the control of motion artifact in studies of functional connectivity. *Neuroimage* **154**, 174 (2017).
- L. Parkes, B. D. Fulcher, M. Yücel, and A. Fornito. An evaluation of the efficacy, reliability, and sensitivity of motion correction strategies for resting-state functional MRI. *NeuroImage* **171**, 415 (2018).
- O. Esteban, C. J. Markiewicz, R. W. Blair, et al. fmriprep: a robust preprocessing pipeline for functional mri. *Nature methods* **16**, 111 (2019).
- D. C. Van Essen, S. M. Smith, D. M. Barch, et al. The wu-minn human connectome project: an overview. *Neuroimage* **80**, 62 (2013).
- R. A. Poldrack, E. Congdon, W. Triplett, et al. A genome-wide examination of neural and cognitive function. *Scientific data* **3**, 160110 (2016).
- K. M. Aquino, B. D. Fulcher, L. Parkes, K. Sabaroeedin, and A. Fornito. Identifying and removing widespread signal deflections from fMRI data: Rethinking the global signal regression problem. *BioRxiv* p. 662726 (2019).
- V. Fonov, A. Evans, R. McKinstry, C. Almli, and D. Collins. Unbiased nonlinear average age-appropriate brain templates from birth to adulthood. *NeuroImage* **47**, Supplement 1, S102 (2009).
- M. F. Glasser, S. N. Sotiropoulos, J. A. Wilson, et al. The minimal preprocessing pipelines for the human connectome project. *NeuroImage* **80**, 105 (2013).
- M. Jenkinson, P. Bannister, M. Brady, and S. Smith. Improved optimization for the robust and accurate linear registration and motion correction of brain images. *NeuroImage* **17**, 825 (2002).
- R. H. R. Pruijm, M. Mennes, D. van Rooij, et al. ICA-AROMA: A robust ICA-based strategy for removing motion artifacts from fMRI data. *NeuroImage* **112**, 267 (2015).
- J. D. Power, M. Plitt, T. O. Laumann, and A. Martin. Sources and implications of whole-brain fMRI signals in humans. *NeuroImage* **146**, 609 (2017).
- J. D. Power, A. Mitra, T. O. Laumann, et al. Methods to detect, characterize, and remove motion artifact in resting state fMRI. *NeuroImage* **84**, 320 (2014).
- M. F. Glasser, T. S. Coalson, J. D. Bijsterbosch, et al. Using temporal ICA to selectively remove global noise while preserving global signal in functional MRI data. *NeuroImage* **181**, 692 (2018).
- L. Griffanti, G. Salimi-Khorshidi, C. F. Beckmann, et al. -based artefact removal and accelerated fMRI acquisition for improved resting state network imaging. *NeuroImage* **95**, 232 (2014).
- M. F. Glasser, T. S. Coalson, E. C. Robinson, et al. A multi-modal parcellation of human cerebral cortex. *Nature* **536**, 171 (2016).
- J. D. Power. Temporal ICA has not properly separated global fMRI signals: A comment on Glasser et al.(2018). *NeuroImage* (2019).
- J. D. Power, M. Plitt, S. J. Gotts, et al. Ridding fMRI data of motion-related influences: Removal of signals with distinct spatial and physical bases in multiecho data. *Proceedings of the National Academy of Sciences* **115**, E2105 (2018).

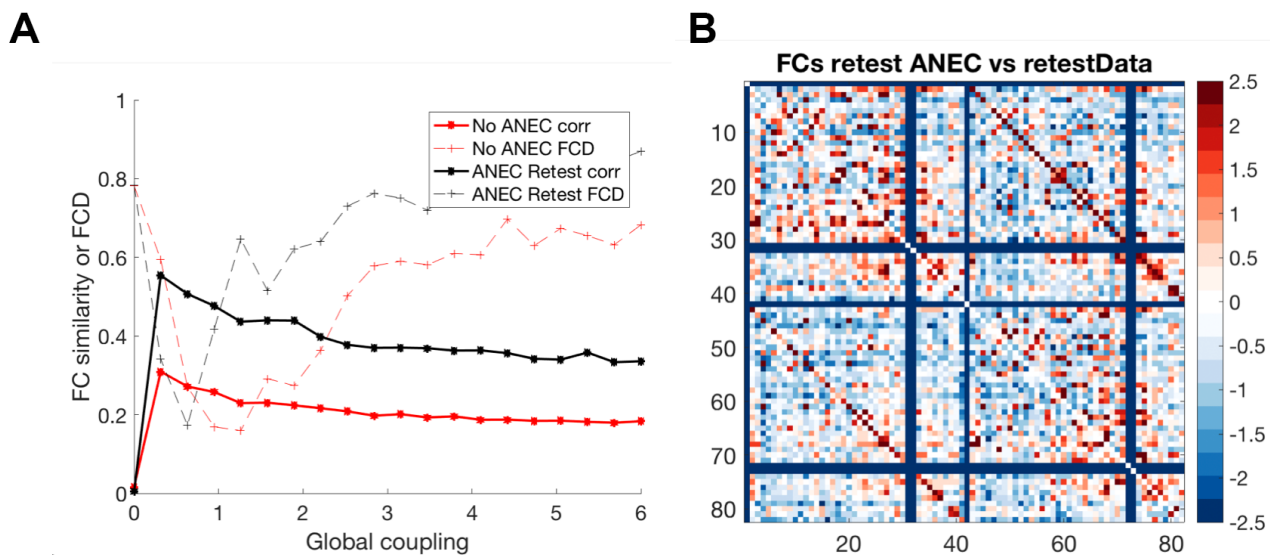


**Fig. 10.** Hopf ANEC

24. T. D. Satterthwaite, D. H. Wolf, J. Loughead, et al. Impact of in-scanner head motion on multiple measures of functional connectivity: relevance for studies of neurodevelopment in youth. *Neuroimage* **60**, 623 (2012).
25. J. D. Power. A simple but useful way to assess fmri scan qualities. *Neuroimage* **154**, 150 (2017).
26. R. M. Birn, J. B. Diamond, M. A. Smith, and P. A. Bandettini. Separating respiratory-variation-related fluctuations from neuronal-activity-related fluctuations in fmri. *Neuroimage* **31**, 1536 (2006).
27. J. D. Power, K. A. Barnes, A. Z. Snyder, B. L. Schlaggar, and S. E. Petersen. Steps toward optimizing motion artifact removal in functional connectivity mri; a reply to carp. *Neuroimage* **76** (2013).
28. K. Murphy, R. M. Birn, D. A. Handwerker, T. B. Jones, and P. A. Bandettini. The impact of global signal regression on resting state correlations: are anti-correlated networks introduced? *Neuroimage* **44**, 893 (2009).
29. Z. S. Saad, S. J. Goots, K. Murphy, et al. Trouble at rest: how correlation patterns and group differences become distorted after global signal regression. *Brain connectivity* **2**, 25 (2012).